J. Fluid Mech. (1993), *vol.* 255, *pp.* 411–435

Nonlinear dynamics of capillary bridges: experiments

By D. J. MOLLOT[1], J. TSAMOPOULOS[2], T.-Y. CHEN[2] AND N. ASHGRIZ[1]

[1] Department of Mechanical Engineering, State University of New York at Buffalo, Buffalo, NY 14260, USA

[2] Department of Chemical Engineering, State University of New York at Buffalo, Buffalo, NY 14260, USA

(Received 26 April 1992 and in revised form 23 March 1993)

An experimental investigation of forced and free oscillations of liquid bridges positioned between two rods of equal diameter is presented. Both the resonance frequencies and damping rates for different aspect ratios of the bridge are reported. The damping rate data of the liquid bridges are obtained by high-speed videography and are the first ever reported. Resonance frequencies for the three modified Reynolds numbers of 14, 295 and 1654, and damping rates for the two modified Reynolds numbers of 14 and 295 are reported. These values of modified Reynolds numbers are generated by using ethylene glycol, distilled water, and mercury in small bridges. Gravitational effects are kept small by reducing the size of the capillary bridge. The internal flow fields of several bridges for different modified Reynolds numbers are described based on high-speed visualization. Experimental results show good agreement with results of linear and nonlinear theory.

1. Introduction

The stability and dynamics of liquid bridges have been of great interest in many natural and industrial processes. Fluid bridges are observed in flow through porous media (Melrose 1966; Zasadzinski *et al.* 1987) and particulates agglomeration (Chen, Tsamopoulos & Good 1992). More recently liquid bridges have been studied because they arise in applications related to materials processing on Earth or in a microgravity environment (Preiser, Schwabe & Scharmann 1983; Brown 1988). Single semiconductor crystals of high purity are produced by melting a polycrystalline feed rod and then allowing it to solidfy into a pure crystal. The quality of the final crystal is intimately dependent on the temperature and concentration uniformity at the solid–liquid interface. Axial oscillation of the capillary bridge may be used to increase the degree of mixing inside it. One of the objectives of this work is to provide further understanding of the flow field inside an axially oscillating liquid bridge. To this end, visualization studies at the particle level are compared with theoretical predictions obtained by tracking Lagrangian particles inside the bridge.

Another application of axially oscillating liquid bridges is in simultaneous measurement of viscosity and surface tension of molten metals and ceramic materials at high temperatures. At present, information on the properties of these materials is limited. At high temperatures most materials become contaminated through contact with the measuring apparatus. Therefore, conventional techniques cannot be used to measure their viscosity and surface tension. The levitated drop technique (Trinh,

Marston & Robey 1988) which avoids the contamination problem, has been developed for measuring the surface tension only. Nevertheless, it requires complicated instrumentation to position the liquid to be tested. The capillary bridge can provide an excellent alternative to such measurements. Tsamopoulos, Chen & Borker (1992) proposed the use of either the static liquid bridge shapes or their resonance frequencies in order to obtain the material surface tension (with and without the presence of gravity). Furthermore, either the resonance frequencies or the damping rates of free oscillating liquid bridges may be used to obtain the viscosity of the liquid.

Although there are numerous reports on the stability of static liquid bridges, the number of studies on the stability and dynamics of oscillating bridges is limited. The pioneering work in this area was conducted by Plateau (1863), Young (1805), and Laplace (1805). Later, Rayleigh (1879, 1892) showed that a stationary liquid cylinder is neutrally stable to a shape disturbance that is infinitesimal in amplitude, sinusoidal in shape, and of wavelength equal to the circumference of the cylinder (Rayleigh limit). More recently, Mason (1970) reported experimental results on the dynamics of capillary bridges. In confirming Plateau's analysis on the stability limit, he observed that it was possible to induce standing waves on capillary bridges by vibrating the upper solid surface. In a more systematic way, Fowle, Wang & Strong (1979) studied capillary bridges between two cylindrical rods when either one or both of them underwent rotation or when the lower one was vibrating vertically. They measured and reported the stability limits and oscillation frequencies of different liquid bridges. They kept the radius of the zone below 2.6 cm, in order to reduce gravitational effects while maintaining a bridge aspect ratio which is large enough for accurate measurements. The experimental data by Fowle *et al.* (1979) are the only data available on the resonance frequencies for 'isolated' liquid bridges. Meseguer (1983), and Rivas & Meseguer (1984) studied the dynamics of axisymmetric bridges immersed in another fluid of the same density. In this case, however, the motion of the liquid in the bridge is affected not only by the solid boundaries (upper and lower) but also by the motion of the outer fluid induced by the moving and deforming liquid/liquid interface. The same technique was applied by Sanz (1985) who used an outer immiscible liquid contained in a cylindrical vessel of radius four times larger than the bridge radius. He reported resonance frequencies and compared them with results from inviscid theory.

More recently, Borkar & Tsamopoulos (1991), and Tsamopoulos *et al.* (1992), motivated by the possibility of deducing material properties from static shapes and dynamic characteristics of liquid bridges, studied their linearized dynamics. Borkar & Tsamopoulos (1991) used a boundary-layer analysis which is applicable for large Reynolds numbers, whereas Tsamopoulos *et al.* (1992) solved the linearized Navier–Stokes equations for a wide range of Reynolds numbers. The nonlinear dynamics of stable bridges were examined by Chen & Tsamopoulos (1993, referred to herein as CT). Further discussion of the nonlinear analysis will be given in the following sections in conjunction with the experimental results.

The objectives of this work are twofold: first, to provide data on both the resonance frequencies in forced oscillations and the damping rates in free oscillations for isolated bridges in air and under standard gravitational conditions; and second, to investigate the flow fields inside the capillary bridges for various conditions. The experimental apparatus and procedures are described in §2. Measured resonance frequencies and damping rates along with comparison with predictions from linear and nonlinear theory are presented in §§3 and 4, respectively. Observations and calculations of the internal flow field are given in §5. Finally, conclusions are drawn in §6.

2. Experimental apparatus and technique

The experiments are performed using the set-up shown in figure 1. This system consists of two metal rods aligned vertically. The bottom rod is fixed and the top one is oscillating. The capillary bridge is formed by injecting liquid (via a syringe) in the gap between the two rods. Controlled excitation of the liquid is achieved by using the solenoid of a 10 in. speaker mounted on top of the apparatus. All critical surfaces of the support structure are machined to ensure that the upper and lower liquid supports are parallel and axially aligned. A short wire stinger connecting the upper support rod and the speaker voice coil compensates for any misalignment between the two. The oscillating upper support rod is kept precisely aligned with the lower rod by securing it through a $\frac{3}{4}$ in. linear sleeve bearing. The system is isolated from high-frequency noise by using rubber pads to mount the speaker on the support structure, and a rubber mat separated the apparatus from the lab bench.

Driving the speaker is a Hewlett Packard 6827A amplifier with a sinusoidal signal input from either a Hewlett Packard 8111A function generator or a Data Translation DT2805 D/A board installed in an AT compatible personal computer. For the damping rate measurements the position of the upper rod as a function of the input signal must be known in order to stop this rod at a desired location. Since the driving system does not have a position feedback loop, the phase lag between the input signal and the upper rod location is needed (Bode phase plot). This phase lag is determined by a GenRad frequency analyser coupled to an accelerometer (Kistler model 8616A500) connected directly to the rod. Once the phase lag data for the system are obtained a polynomial is used to approximate the rod position as a function of the input signal. This polynomial is then used in the computer driver program to relate the speaker input voltage to the position of the oscillating upper rod. The sinusoidal motion of the upper rod is verified for all the frequencies reported here.

The volume of liquid in the bridge is approximated by that of a cylinder with radius equal to that of the rod tip and length equal to the separation of the rods before excitation. The length is measured using a vernier height gauge and verified photographically with a reference scale. The radius of both rods for all of our experiments is 0.096 cm. The diameter and length of the bridges are selected in order to reduce the bulging induced by gravity while keeping the bridge size and excitation frequencies within limits of available equipment. Because of the relatively high vapour pressure of distilled water, significant mass losses could occur during the course of the experiments. To avoid this the vapour pressure of the liquid around the bridge is increased by placing a pool of distilled water directly below the liquid column. The same is done with ethylene glycol. Liquids in the columns are frequently changed (generally just before each experiment) to reduce contamination problems, and they are monitored for losses due to evaporation. The ethylene glycol and water bridges are supported using a set of aluminium rods. Both liquids wet the two rods well and seemed to adhere to their edges. No motion of the three-phase contact line was detected even at a 70-fold magnification.

The mercury bridge required its own copper support rods with a mercury/copper amalgam on the contact surface. To form the amalgam the surface contamination on the copper is removed by immersing it in a pool of hydrochloric acid. Near the bottom of the pool is a puddle of mercury which is used to produce an amalgam with the copper rod as the two are brought to contact. To isolate the desired mercury/copper interface and keep the mercury from creeping down (or up) the sides of the rods, the vertical surfaces of the rods are coated with wax. Nevertheless, the wax seal is not

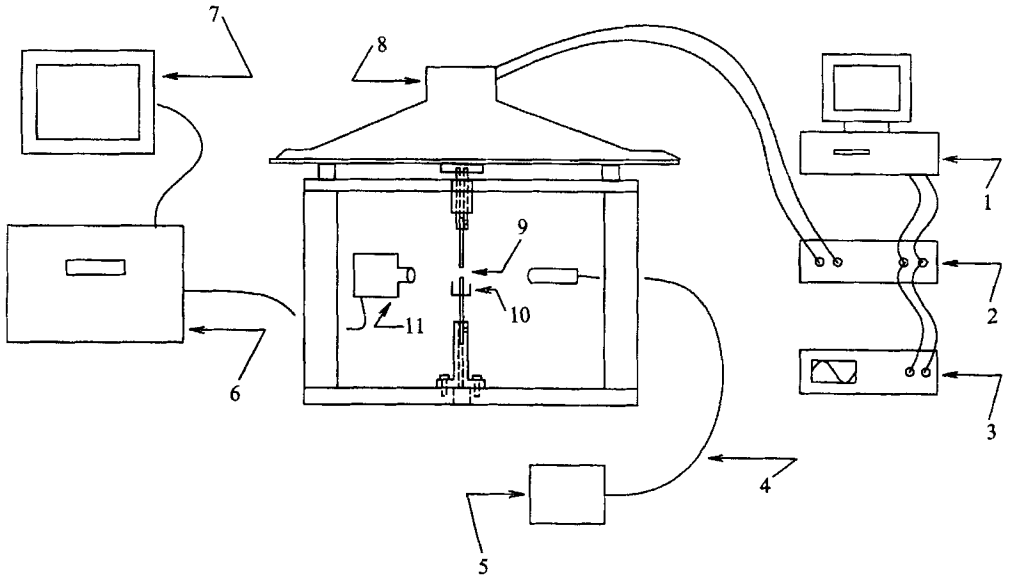

FIGURE 1. Schematic (not to scale) of the experimental arrangement. (1) Personal computer with DT2805 digital-to-analog board, (2) power amplifier, (3) function generator, (4) fibre-optic cable for strobe light source, (5) strobe light source (triggered by the high-speed video), (6) high-speed video tape drive and CPU, (7) monitor, (8) mechanically linked speaker/driver, (9) location of liquid bridge, (10) cup with liquid to prevent excessive evaporation, (11) high speed camera.

perfect and the mercury bridges are more prone to distortions very close to the three-phase contact lines.

The frequency and damping rate data are obtained by a high-speed video camera (EktaPro 1000 manufactured by Kodak). This system is capable of recording up to 1000 full frame pictures per second using a 240 by 192 sensor array (pixels) video camera. Since the image is digitized the liquid surface position can be determined to within the pixel resolution. The exposure times are limited to 11 μs by using a strobe light. The high-speed video camera is used both for the frequency and damping rate measurements. The high-speed visualization is essential for the damping rate measurements since time-resolved recording of the bridge surface amplitude is needed. The internal flow field of the bridge is recorded using a conventional 35 mm camera, which has a better resolution than the high-speed video camera. In these experiments liquid columns are seeded with aluminium oxide powder and are illuminated using two 5 mW He–Ne lasers positioned at close to a 90° angle with respect to the camera.

3. Resonance frequency of liquid bridges

Resonance frequencies of the first and second modes of liquid bridges with different aspect ratios are obtained using three different fluids, namely water, ethylene glycol, and mercury. The physical properties of these liquids are listed in table 1. After the liquids are injected in the space between the rods, the upper supporting rod is brought into sinusoidal oscillation with an amplitude $\bar{A}$ at or near the first resonance frequency of each bridge via the solenoid of the driving speaker. In order to find the resonance frequency, the linear eigenfrequencies are used to obtain the approximate starting values. Linear eigenfrequencies are calculated by Tsamopoulos *et al.* (1992) as a function of bridge geometry characterized by the aspect ratio, the modified Reynolds

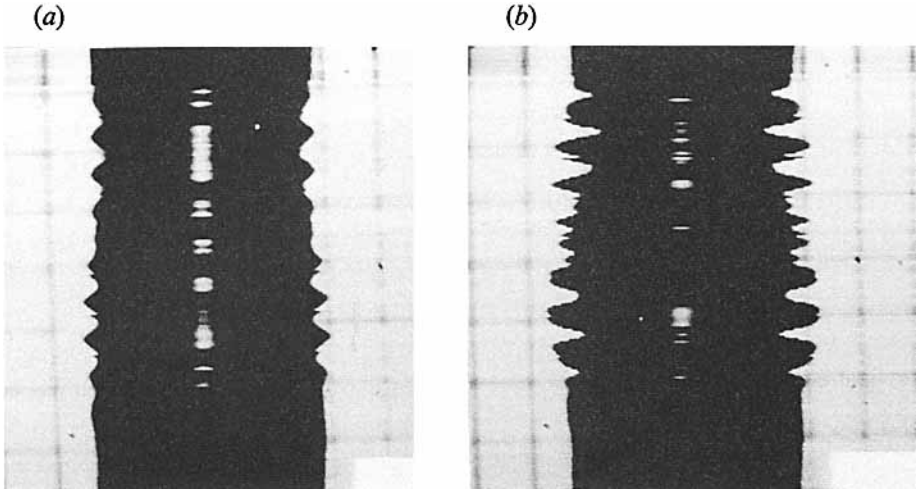

FIGURE 2. Water column showing segmented EktaPro image for $\Lambda = 0.371$, $B = 0.339$. The bridge is excited (*a*) below its first mode resonance frequency, $\bar{\omega} = 465$ rads/s and (*b*) at first mode resonance frequency $\bar{\omega} = 478$ rads/s.

Liquid	ρ(gm/cm^3)	γ(dynes/cm)	μ(gm/cm s)
Ethylene glycol	1.1	48.2	16.2×10^{-2}
Water	1.0	72.0	0.89×10^{-2}
Water[1]	1.0	72.6	1.00×10^{-2}
Mercury	13.63	484	1.53×10^{-2}

[1] Values used by Fowle *et al.* (1979).

TABLE 1. Physical properties of ethylene glycol, water, and mercury at temperature of 25 °C

number, and the Bond number. The aspect ratio is defined as $\Lambda = \bar{R}/\bar{L}$, where $\bar{R}$ and $\bar{L}$ are the bridge radius and length, respectively. The modified Reynolds number is defined as $Re = (\rho\gamma\bar{R})^{\frac{1}{2}}/\mu$, where ρ and μ are the liquid density and viscosity, respectively, and γ is the surface tension of each liquid/gas system. The gravitational Bond number is defined as $B = \rho g\bar{R}\bar{L}/\gamma$, where g is the gravitational acceleration. Variables with overbars indicate dimensional quantities.

The actual resonance frequency is then determined to within a 2–3 Hz by adjusting the output frequency from either the D/A board or the function generator until the amplitude of the radial deflection of the liquid bridge reaches a maximum. The function generator is used when only the frequency data, and not the damping rates, are of interest. In order to experimentally determine the resonance frequencies, oscillating bridges are viewed live on the video monitor while operating at 1000 frames per second. Typical images, observed on the video monitor, of the oscillating water bridges at slightly off resonance and at resonance frequencies for first and second modes are shown in figures 2 and 3, respectively. The ripple pattern on the edges of the column are due to the particular way in which the video camera displays and records images.

As noted earlier, the sensor array of the EktaPro has 240 columns and 192 rows of photo capacitive cells that convert light focused by the lenses into measurable electrical charges. The charge that is stored by each cell is picked up once per frame by a

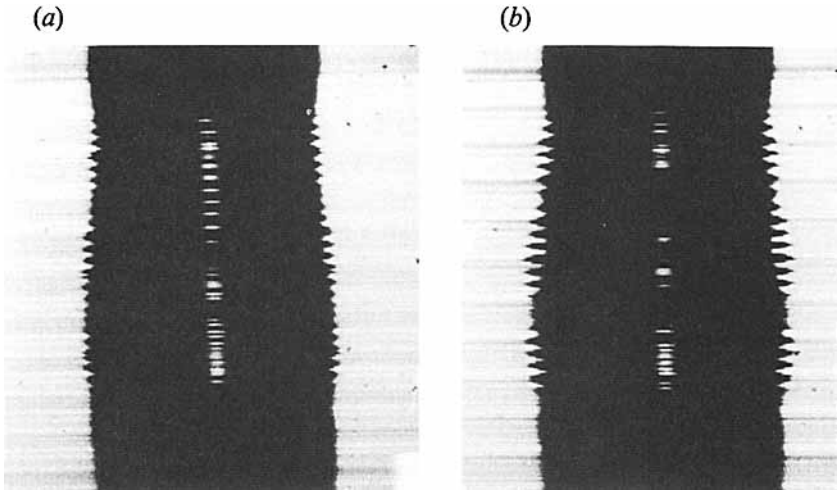

FIGURE 3. Water column showing segmented EktaPro image for $A = 0.378$, $B = 0.332$. The bridge is excited (*a*) above its second mode resonance frequency, $\bar{\omega} = 1301$ rads/s and (*b*) at its second mode resonance frequency, $\bar{\omega} = 1232$ rads/s.

scanning process which takes the charge from each cell in the array one after another. Since each scanning cycle must read 46080 pixels (240×192) before starting again, scanning the sensor one pixel after another limits the framing rate to about 60 frames per second. To achieve a frame rate of 1000 frames per second it is necessary to scan the array 16 times faster. The EktaPro achieves this speed increase by scanning sixteen consecutive rows of pixels simultaneously. Each group of these 16 simultaneously read rows is called a block and there are 12 blocks to a frame. In this manner 1000 frames per second can be sent to the recording tape drive and to a memory buffer. The buffer is read by the graphics card and displayed on the monitor at a rate of once every $\frac{1}{30}$ s. The graphics card reads the first row of each of the blocks in the data buffer and then allows the data buffer to be rewritten by the camera before reading the second row in each of the blocks. In the time it takes for the graphics board to read one line in each block, the camera has twice had a frame worth of data available to rewrite the buffer. Since significant fluid motion has occurred within each data buffer rewrite, the image displayed on the monitor shows the apparent discontinuities seen in figures 2 and 3. The advantage of determining the resonance frequency from these fragmented images is that for forcing frequencies greater than 30 Hz the radial amplitudes for the entire bridge for at least one complete cycle are seen in each frame. An additional benefit is that the damping experiment may be performed immediately following this rapid visual determination of the resonance frequency by toggling the camera into record mode and initiating the column stopping sequence.

Tables 2 and 3 show the results for the first and second mode frequencies, respectively, under various conditions. The dimensionless forcing amplitude is defined as $\alpha = \bar{A}/\bar{R}$. Since the characteristic time of the flow in the bridge may be related to the fluid properties, the forcing frequency, $\bar{\omega}$, is made dimensionless as

$$\sigma = \bar{\omega}(\rho \bar{R}^3/\gamma)^{\frac{1}{2}}. \tag{3.1}$$

The results by Fowle *et al.* (1979) for water are also included in these tables for comparison. Data on amplitude of excitation are not reported by these authors.

In order to relate the accuracy of the frequency measurements, $\Delta\bar{\omega}$, to that of the viscosity predictions, $\Delta\mu$, the following relation is used: $\Delta\bar{\omega} = (\gamma \Delta Re\, \Delta\sigma)/(\bar{R}\, Re^2\, \Delta\mu)$.

Liquid	$\bar{L}$(mm)	Λ	$\bar{A}$(mm)	α	$\bar{A}/\bar{L}$	B	$\bar{\omega}$(rads/s)	σ Ex	σ LT	σ NT
Ethylene	1.10	0.873	0.013	0.013	0.012	0.236	1508	6.78	—	—
Glycol	1.43	0.674	0.025	0.026	0.017	0.306	1068	4.80	—	—
($Re = 14$)	1.70	0.565	0.063	0.065	0.037	0.365	754	3.39	—	—
	2.05	0.468	0.063	0.065	0.031	0.440	471	2.12	—	—
	2.10	0.457	0.038	0.039	0.018	0.451	440	1.98	—	—
	2.17	0.442	0.096	0.100	0.044	0.467	496	2.21	—	—
	2.27	0.423	0.092	0.096	0.041	0.487	452	2.03	—	—
	2.34	0.410	0.125	0.130	0.053	0.502	427	1.91	—	—
	2.36	0.407	0.105	0.109	0.044	0.506	421	1.88	2.131	1.823
	2.47	0.389	0.115	0.120	0.047	0.530	415	1.85	—	—
	2.60	0.369	0.105	0.109	0.040	0.558	371	1.66	—	—
	2.62	0.366	0.149	0.155	0.057	0.563	327	1.47	1.717	1.456
	2.71	0.354	0.125	0.130	0.046	0.581	346	1.55	—	—
	2.73	0.352	0.155	0.161	0.057	0.586	352	1.59	—	—
	2.83	0.339	0.115	0.120	0.041	0.607	320	1.43	—	—
	2.88	0.333	0.165	0.172	0.057	0.618	314	1.41	—	—
	2.99	0.321	0.185	0.193	0.062	0.641	283	1.27	—	—
	3.15	0.305	0.225	0.234	0.071	0.677	214	0.96	—	—
Mercury	1.93	0.503	0.042	0.044	0.022	0.517	534	2.71	—	—
($Re = 1654$)	2.44	0.398	0.050	0.052	0.020	0.654	371	1.88	—	—
Water[1]	1.25	0.768	0.03	0.026	0.020	0.164	1678	5.88	—	—
($Re = 295$)	1.45	0.662	0.05	0.052	0.034	0.190	1118	3.92	—	—
	1.78	0.539	0.02	0.021	0.011	0.233	930	3.26	3.677	—
	1.78	0.539	0.02	0.021	0.011	0.233	898	3.15	—	—
	1.81	0.530	0.02	0.021	0.011	0.237	811	2.84	3.564	—
	1.89	0.508	0.02	0.021	0.011	0.247	842	2.95	—	—
	2.05	0.468	0.03	0.031	0.015	0.268	741	2.60	—	—
	2.17	0.442	0.03	0.031	0.014	0.284	666	2.32	—	—
	2.35	0.409	0.06	0.063	0.026	0.308	597	2.10	—	—
	2.48	0.387	0.06	0.063	0.024	0.325	440	1.54	1.871	—
	2.62	0.366	0.05	0.052	0.019	0.343	484	1.70	1.688	—
	2.63	0.365	0.04	0.042	0.015	0.343	484	1.70	1.685	—
	2.85	0.337	0.11	0.115	0.039	0.372	383	1.34	—	—
	3.16	0.304	0.10	0.104	0.032	0.413	314	1.10	—	—
	3.50	0.274	0.04	0.042	0.011	0.458	251	0.88	—	—
	3.73	0.257	0.18	0.188	0.021	0.488	232	0.82	0.661	—
Water[2#]	1.12	0.592	—	—	—	0.100	1693	3.37	—	—
($Re = 219$)	1.53	0.430	—	—	—	0.136	1054	2.10	—	—
	2.10	0.314	—	—	—	0.187	612	1.22	—	—
	2.31	0.286	—	—	—	0.206	474	0.943	—	—
Water[3#]	1.30	0.974	—	—	—	0.223	1601	8.50	—	—
($Re = 304$)	1.67	0.764	—	—	—	0.286	1167	6.20	—	—

TABLE 2. Bridge geometry, excitation amplitude, fluid parameters and corresponding resonance frequency of the first mode. Dimensionless experimental (Ex) and theoretical values according to linear (LT) from Tsamopoulos *et al.* (1992) and nonlinear theory (NT) from CT are also shown. $\bar{R} = 0.96$ mm for ethylene glycol and mercury, whereas for water superscripts 1, 2 and 3 indicate $\bar{R} = 0.96$, 0.66, and 1.27 mm respectively, and * indicates data from Fowle *et al.* (1979).

Liquid	$\bar{L}$(mm)	Λ	$\bar{A}$(mm)	α	$\bar{A}/\bar{L}$	B	$\bar{\omega}$(rads/s)	σ
Water[1]	1.25	0.768	*	*	—	0.163	3537	12.40
(Re = 295)	1.40	0.686	*	*	—	0.183	2739	9.61
	1.53	0.630	*	*	—	0.199	2463	8.64
	1.68	0.573	*	*	—	0.219	2199	7.71
	1.70	0.565	*	*	—	0.222	2004	7.03
	1.80	0.533	*	*	—	0.235	1791	6.28
	1.95	0.492	0.025	0.026	0.013	0.255	1571	5.51
	2.05	0.468	0.075	0.078	0.037	0.268	1602	5.62
	2.15	0.447	*	*	—	0.281	1407	4.93
	2.20	0.436	0.025	0.026	0.011	0.288	1407	4.93
	2.28	0.422	*	*	—	0.297	1445	5.07
	2.30	0.417	*	*	—	0.301	1326	4.65
	2.40	0.400	0.025	0.026	0.010	0.314	1294	4.54
	2.55	0.376	0.050	0.052	0.020	0.333	1018	3.57
	2.75	0.349	0.075	0.078	0.027	0.360	911	3.19
	2.95	0.325	0.100	0.104	0.034	0.386	829	2.91
	3.18	0.302	0.075	0.078	0.024	0.415	741	2.60
	3.23	0.298	0.075	0.078	0.023	0.422	704	2.47
	3.45	0.278	0.100	0.104	0.029	0.451	597	2.10
	4.13	0.233	0.150	0.156	0.036	0.539	434	1.52
Water[2*]	2.10	0.314	—	—	—	0.187	1503	2.99
(Re = 219)	2.65	0.249	—	—	—	0.236	948	1.89
Water[3*]	1.91	0.665	—	—	—	0.328	1854	9.85
(Re = 304)	2.57	0.494	—	—	—	0.441	1135	6.03
Water[4*]	3.17	0.783	—	—	—	1.060	849	12.31
(Re = 424)	3.57	0.694	—	—	—	1.196	767	11.12

* Below measurement tolerance, $\bar{A} < 0.025$ mm or $\alpha < 0.026$.

TABLE 3. Bridge geometry, excitation amplitude, fluid parameters and corresponding resonance frequencies of the second mode. (Superscripts 1, 2, 3 and 4 indicate $\bar{R}$ = 0.96, 0.66, 1.27, and 2.48 mm respectively and * indicates data from Fowle *et al.* (1979).

This equation is derived by relating the change in frequency to the change in the modified Re, ΔRe, assuming that other parameters remain constant. Using the calculated data of CT (table 2 of CT) for low Re ($Re \leqslant 50$), it can be obtained that approximately 20 rads/s precision is needed to provide a 1 cP precision in determining the viscosity. Higher accuracy in frequency measurements is needed for higher-Re liquids. The precision of the frequency measurements in the present experiments (Re = 14, 295, and 1654) is about 20 rads/s ($\approx$ 3 Hz) for frequencies below 900 rads/s and increases to a maximum of 40 rads/s at higher frequencies. This indicates that the measurement technique presented here is of sufficient accuracy for low-Re liquids to resolve 1 cP variation in viscosity.

Resonance frequencies for five Reynolds numbers and for both the first and second modes are plotted in figure 4. For comparison the linear theory of Tsamopoulos *et al.* (1992) is used to calculate first and second mode excitation frequencies for bridges at Reynolds numbers of 10 and 500. The predicted values are connected by solid (Re = 500) or dashed (Re = 10) lines to form continuous curves. The results show that the resonance frequencies increase with the aspect ratio. The weak dependence on Reynolds number seen in the linear prediction is on the order of the scatter and in the scale of this plot cannot be detected. As noted above however, the data for ethylene glycol are measured with sufficient accuracy, and when amplitude effects are accounted

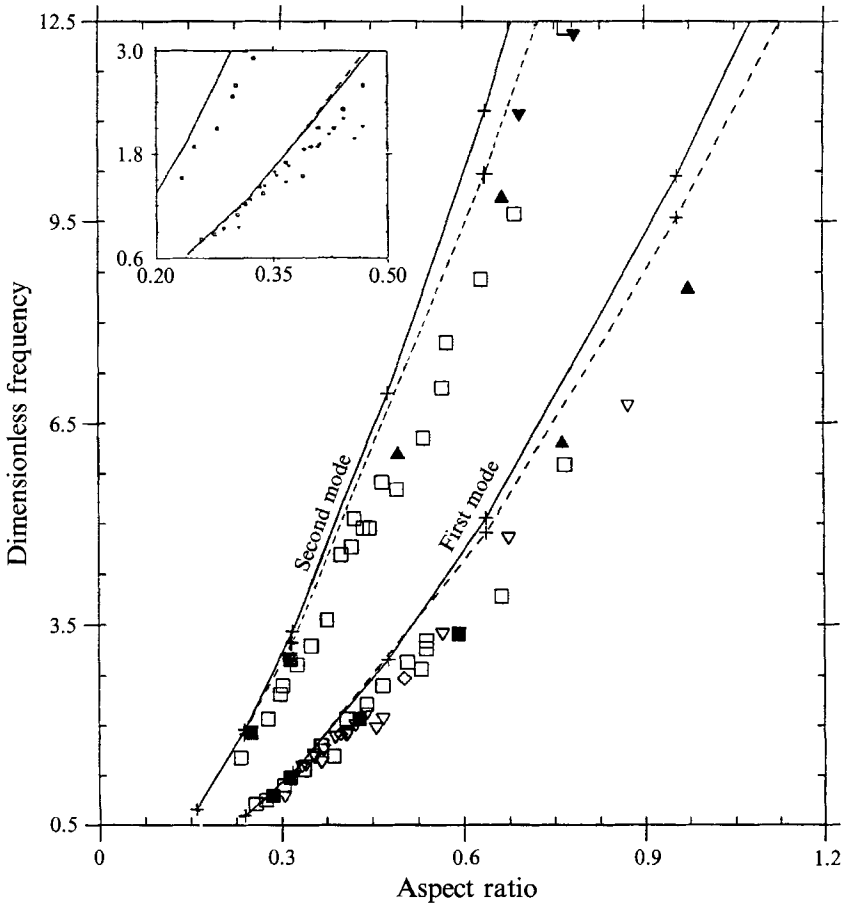

FIGURE 4. Resonance frequency for ethylene glycol, water, and mercury. Symbols indicate results for water (■, □, ▲, ▼) with $Re = 219$, 295, 304, and 424, ethylene glycol (▽) with $Re = 14$, and mercury (◇) with $Re = 1654$. The lines indicate theoretical results based on linear theory for $Re = 500$ (solid line) and $Re = 10$ (dashed line). Filled symbols are data from Fowle *et al.* (1979).

for they match predictions from the nonlinear theory. This is further discussed below. In general, data of the first mode fall an average of 19% below the linear prediction. Resonance frequencies for the longer (lower aspect ratio) bridges tend to approach the theoretical values. This can be explained by noting that the volume displacement relative to the total bridge volume, for the same excitation amplitude, is larger for the shorter bridges than the longer ones. Therefore, in shorter bridges, which also have higher resonance frequencies, relatively stronger convective fields are established. The enhanced convective fields increase the viscous damping, and reduce the resonance frequency relative to that predicted by the linear theory where convective terms are neglected altogether. Data for the first mode for $\Lambda > 0.5$ fall an average of 22% below the linear prediction while data for $0.4 < \Lambda < 0.5$ and $\Lambda < 0.4$ fall 18% and 16% below the predicted values, respectively. This trend is not seen for bridges excited at the resonance frequency of the second mode where the data remain consistently 21% below the linear prediction.

Results from the nonlinear calculations according to CT are also compared to two of the experiments with ethylene glycol bridges as shown in table 2. Very briefly, for these nonlinear calculations the Navier–Stokes equations are solved numerically for an

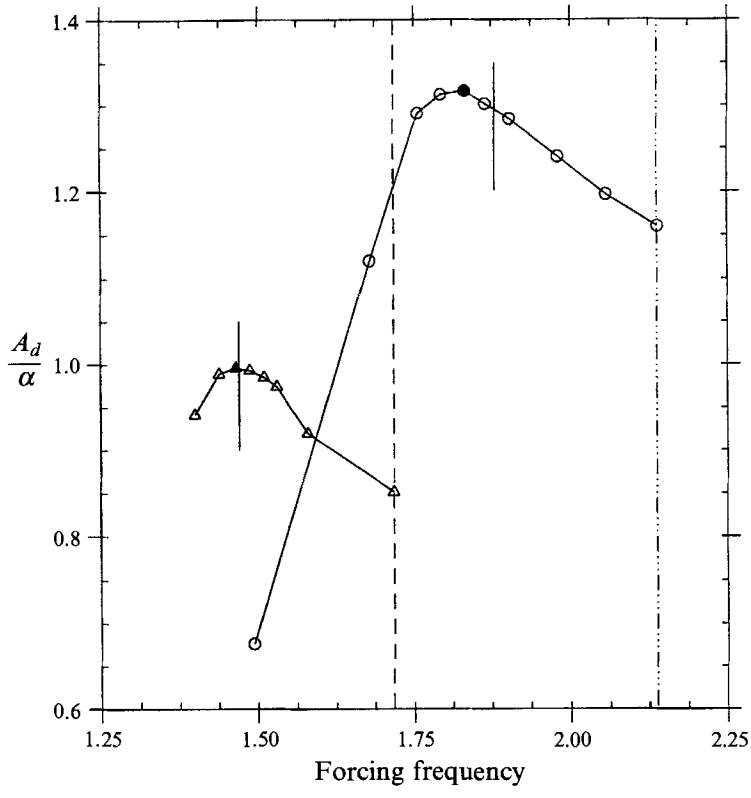

FIGURE 5. Response of normalized overall amplitude, A_d, to different forcing frequencies for two different experiments with ethylene glycol, $Re = 14$. Conditions are $\alpha = 0.155$, $A = 0.366$, $B = 0.563$ (△, nonlinear or ——, linear analysis); $\alpha = 0.109$, $A = 0.407$, $B = 0.506$ (○, nonlinear or – · · · –, linear analysis). Filled symbols indicate resonant frequencies and dashed vertical lines indicate the corresponding linear eigenfrequencies. The experimentally determined frequencies are indicated by the short solid lines.

oscillating liquid bridge. Galerkin/finite-element methodology is used for discretization in space and implicit finite differences for discretization in time. Calculations could only be carried out for ethylene glycol which has $Re = 14$. For other fluids tested here, which have $Re > 100$, the oscillatory boundary layer that arises at the solid/liquid interfaces, the internal layers, and complicated flow recirculation patterns require a much finer finite-element mesh for their accurate resolution. This makes the computational time needed to carry out these extensive calculations prohibitively large. In these calculations the overall amplitude is defined by

$$A_d = \int_0^{1+G(t)} |f(z,t) - 1| \, dz, \tag{3.2}$$

where $1 + G(t)$ is the time-varying distance of the upper rod from the lower one made dimensionless by $\bar{L}$, and $f(z, t)$ is the distance of the side surface from the axis of symmetry of the bridge made dimensionless by $\bar{R}$. In order to obtain the resonance frequency theoretically, A_d normalized by α is plotted versus forcing frequency after a steady oscillating motion is established (CT). Figure 5 shows such a plot for two different aspect ratios for ethylene glycol ($Re = 14$). The maximum of each curve (filled symbols) indicates theoretical nonlinear resonance conditions while the short solid vertical lines show the measured resonance frequencies of the corresponding

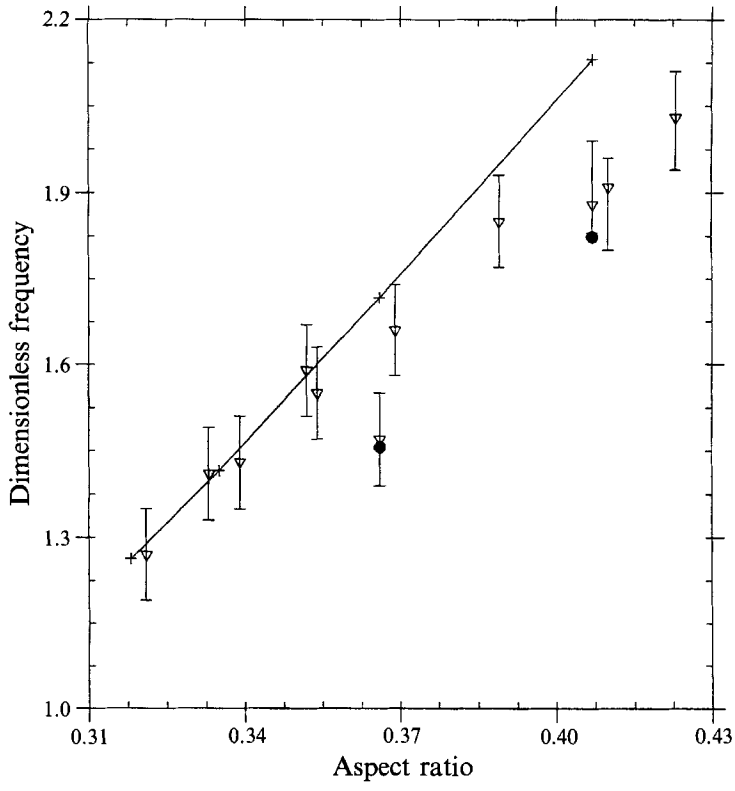

FIGURE 6. Resonance frequency for ethylene glycol as a function of aspect ratio. Symbols indicate experimental results (▽), results from nonlinear theory (●), and results from linear theory (+). Linear theoretical results are connected with a continuous curve.

experimental liquid bridges. The linear eigenfrequencies are indicated in figure 5 by the dashed vertical lines. The experimental points fall in between the linear and nonlinear predictions and their deviation from the nonlinear prediction is much smaller than that from the linear prediction (less than 3%, which is within the uncertainty of the measurement). Clearly, there is a pronounced improvement in the prediction of the experimental results using the nonlinear theory.

Figure 6 and table 2 show experimental values of resonance frequencies for ethylene glycol along with the predicted values from linear theory (Tsamopoulos *et al.* 1992) as a function of aspect ratio. The nonlinear calculations for the two data points reported above are also shown. The scatter in the experimental points is due to both experimental uncertainty and their dependence on the forcing amplitude, which varies from point to point (see table 2). It should be noted that longer bridges (smaller A) than those shown could not be sustained due to the stability limit when $B \neq 0$, whereas shorter ones (larger A) required such large forcing frequencies and exhibited such fast damping that accurate measurements of damping rates exceeded the limitations of available equipment.

4. Damping rates of liquid bridges

In order to obtain damping rates of liquid bridges for various conditions the liquid column is first brought into resonance and is run for a few hundred forced oscillations so that all initial transients are dissipated. Then the top rod is suddenly stopped at the

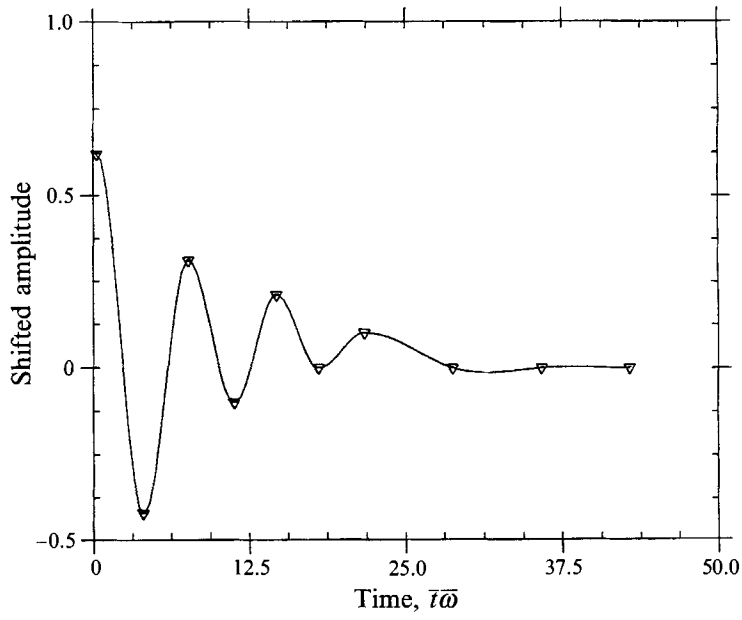

FIGURE 7. Evolution of the shifted point amplitude, $[A_p(t)-A_p(t_\infty)]/\alpha$, at a position 75% of the column height for an ethylene glycol bridge in free oscillation after resonance was achieved. Conditions are $Re = 14$, $\alpha = 0.193$, $A = 0.321$, and $B = 0.642$.

top of the stroke and the motion of the liquid is continuously recorded at 1000 frames per second until all oscillations are damped out. The damping rate data are later extracted from frame-by-frame examination of the recorded images of the liquid surface amplitude. Disturbances of the column during switching from forced to free oscillations are eliminated by stopping the top rod at its maximum distance from the bottom one where the forcing velocity is zero. An instantaneous transition from forced to free oscillation is possible at this point by replacing the sinusoidal excitation with an appropriate DC voltage. The D/A board is programmed to stop outputting a sine function at a keyboard command and replace it with a constant voltage of suitable magnitude to hold the rod at the maximum height generated by the preceding sine wave. After the command is given to hold the voltage, the D/A board waits until the rod is at its maximum height before switching to constant voltage.

The surface deflection amplitude, A_d, which is defined by (3.2), is approximated by the deflection amplitude of a single point on the surface (designated A_p). Therefore, the damping information is deduced from the recorded images by following the motion of a selected point on the surface of the bridge. For most experiments in the first mode, deflections of the free surface of the bridge are close to a maximum at three-quarters of the column height from the bottom boundary. Therefore, this point was chosen to facilitate more accurate measurements of the amplitude from still frames. By recording the location of this point at the extremes of its motion and the corresponding frame number, which is directly related to elapsed time, the rate of damping of the freely oscillating bridge is determined. The presence of gravity distorts the shape of even static bridges. This is accounted for in fitting the experimental damping data to an exponential function of the following form:

$$\bar{A}_p(\bar{t}) = [\bar{A}_p(\bar{t}_1)-\bar{A}_p(\bar{t}_\infty)]\,\mathrm{e}^{-(\bar{t}-\bar{t}_1)\,\bar{\sigma}_D}+\bar{A}_p(\bar{t}_\infty). \tag{4.1}$$

In this expression, $\bar{A}_p$ is the oscillation amplitude in mm during damping of the

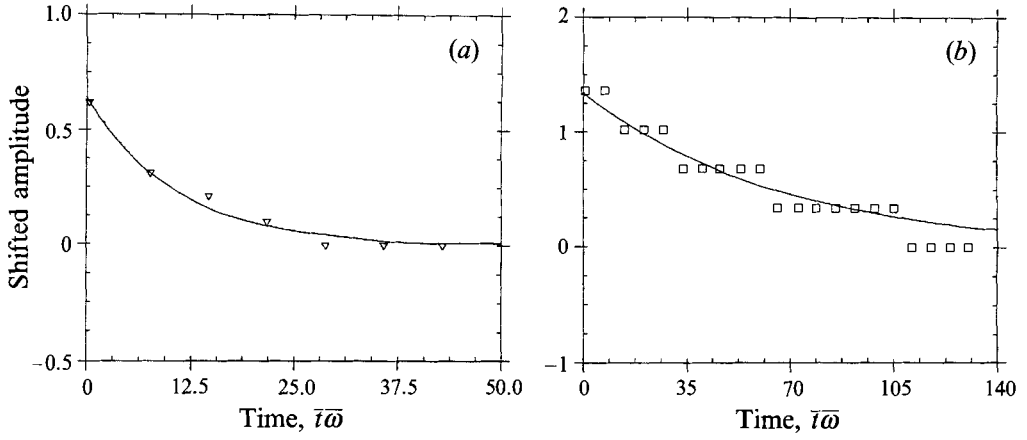

FIGURE 8. Evolution of the maxima of point amplitude, A_p, for ethylene glycol and water bridges in free oscillation after resonance is achieved: (*a*) ethylene glycol bridge with exponential fit to first two maxima, $Re = 14$, $\alpha = 0.193$, and $\Lambda = 0.321$; (*b*) water bridge with exponential fit to all points by applying linear regression to log of equation (4.1), $Re = 295$, $\alpha = 0.063$, and $\Lambda = 0.409$.

examined point at any time ($\bar{t}$), at the first time it is achieved ($\bar{t}_1$), and after motion has ceased ($\bar{t}_\infty$); $\bar{\sigma}_D$ is the dimensional damping rate in 1/s which may be made dimensionless with respect to either the fluid properties, or the forcing frequency $\bar{\omega}$, i.e.

$$\sigma_D = \bar{\sigma}_D\left(\frac{\rho\bar{R}^3}{\gamma}\right)^{\frac{1}{2}} \quad \text{or} \quad \sigma_D^* = \frac{\bar{\sigma}_D}{\bar{\omega}} = \frac{\sigma_D}{\sigma}. \tag{4.2}$$

Figure 7 shows the variation in time (made dimensionless by the forcing frequency $\bar{\omega}$) of the shifted point amplitude, $[A_p(t) - A_p(t_\infty)]/\alpha$, made dimensionless by the bridge radius and normalized by $\alpha = 0.193$ for ethylene glycol with $\Lambda = 0.321$ and $B = 0.641$. It can be readily seen that the motion rapidly damps out and only 3–4 maxima can be sufficiently differentiated from the shifted final value of A_p. This is the reason why it was necessary to use such large amplitudes for these experiments, see table 2. The maximum positive values of the shifted amplitude are plotted in figures 8(*a*) and 8(*b*) for typical ethylene glycol and water bridges, respectively. For the ethylene glycol bridges the exponential is fit through the first two points since these experience the largest displacement amplitudes and are therefore most accurately read. Similarly, the nonlinear calculation of CT, used the first two maxima of A_d to calculate σ_D. As discussed in CT the range of variation of the damping rate is bounded by the initial maximum value and the results from linear analysis. However, the maximum value is taken as a characteristic of the finite-amplitude oscillation.

This approach is not possible for the water bridges which have higher Re. The initial peak-to-peak deflection of the water bridge is approximately the same as that recorded for the highest surface amplitude in the bridges of ethylene glycol (≈ 7 pixels). However, because the water bridges require many more cycles to damp out, and due to the limited pixel resolution of the EktaPro, the amplitudes for two or more consecutive pictures appear the same, as shown in figure 8(*b*). Since it is not meaningful to use the first two points to determine the damping rate in these bridges, the average damping rate is calculated by a least-squares fit of the logarithm of (4.1) using all the data (solid line in figure 8*b*).

Experimental damping rates as a function of aspect ratio, for water and ethylene glycol, are given in table 4 and plotted in figure 9. Motion of less intensity and fewer

measurable A_p maxima of the ethylene glycol column, coupled with the limited resolution of the camera, lead to large uncertainties in amplitude measurement. The error bars shown in figure 9 are calculated based on errors due to pixel resolution during data collection. Data with uncertainties greater than $\Delta\sigma_D = 0.2$ have not been plotted. As expected the damping rates for lower-Re bridge of ethylene glycol ($Re = 14$) is larger than that of water bridges with $Re = 295$. Also, the rate of increase in damping rate with aspect ratio is higher for ethylene glycol than water bridges. There is a clear distinction between the data for the two fluids, making measurements of damping rates more effective than measurements of resonance frequencies for the determination of the fluid viscosity.

In order to compare the theoretical calculations with the experimental data the nonlinear calculations reported by CT are modified to accurately simulate the experimental procedure. As mentioned above, in switching from forced to free oscillations it was necessary to stop the upper rod when it was located at the uppermost point of its oscillatory trajectory. Clearly, this would modify the bridge geometry at final equilibrium. This procedure, however, has the advantage that the motion of the liquid prior to switching to free oscillations is well known. This is in contrast to the situation with the motion stopping at the original location in which case the phase in the oscillation cycle must be recorded since it affects the damping rate when gravity is present (see CT). Nevertheles, predictions reported in CT assume that the upper rod returns to its original location before its motion stops. According to those calculations nonlinear damping rates should be significantly higher than the corresponding linear ones. In order to properly compare experimental results and nonlinear theory, finite-element calculations are repeated with the upper rod stopping at its point of maximum separation after steady oscillations have been achieved. Surprisingly, these modified nonlinear calculations from ethylene glycol result in nonlinear damping rates that can be well approximated by their corresponding linear values (see table 4). It is expected therefore that nonlinear data on damping rates will be generally less dependent on the amplitude of oscillation than nonlinear data for resonance frequencies.

The calculated values for selected ethylene glycol bridges ($Re = 14$) based on the above-mentioned modification of the nonlinear analysis of CT are shown in figure 9 by the filled symbols. For comparison the linear calculations following the method of Tsamopoulos *et al.* (1992) are also given in table 4 and are plotted as solid curves in figure 9. The dashed lines are best fit curves to the experimental data and are calculated using a linear regression technique. It may be observed that experimental values for water fall slightly above the theoretical ones, whereas the ethylene glycol data are scattered above and below the linear prediction.

Furthermore, the earlier conjecture that the dependence of the damping rate on amplitude will be weaker is indeed observed. This justifies the utilization of a linear regression technique to fit curves through the experimental data irrespective of values of α. The slopes of these lines are approximately 25% greater (22% for ethylene glycol and 26% for water) than the corresponding curves calculated using the linear theory. The growing deviation between the experimental data and the linear prediction as the bridge length decreases is due to the increased significance of inertia as the relative excitation amplitude becomes larger. This increases the energy dissipation rate of the bridge resulting in the larger damping coefficient. A similar effect was noted in §3 for bridges in forced oscillation. The two damping coefficients calculated using the nonlinear theory of CT also predict a higher damping rate than the linear calculation. These calculated points fall within the uncertainty of the corresponding experimental data.

Liquid	B	Λ	α	$\bar{\sigma}_D$	σ_D Ex	σ_D LT	σ_D NT
Ethylene	0.467	0.442	0.100	48	0.208	—	—
Glycol	0.487	0.423	0.096	50	0.240	—	—
($Re = 14$)	0.506	0.407	0.109	54	0.309	0.234	0.245
	0.502	0.410	0.130	43	0.242	—	—
	0.530	0.389	0.120	47	0.173	—	—
	0.558	0.369	0.109	36	0.177	—	—
	0.563	0.366	0.155	27	0.091	0.183	0.212
	0.581	0.354	0.130	32	0.161	—	—
	0.586	0.352	0.161	28	0.235	—	—
	0.607	0.339	0.120	36	0.187	—	—
	0.618	0.333	0.172	23	0.105	—	—
	0.641	0.321	0.193	29	0.136	—	—
Water	0.233	0.539	0.021	14	0.052	0.029	—
($Re = 295$)	0.233	0.539	0.021	16	0.054	—	—
	0.237	0.530	0.021	22	0.083	0.028	—
	0.247	0.508	0.021	16	0.059	—	—
	0.268	0.468	0.031	16	0.047	—	—
	0.284	0.442	0.031	13	0.050	—	—
	0.308	0.409	0.063	9	0.032	—	—
	0.325	0.387	0.063	7	0.020	0.011	—
	0.343	0.366	0.052	8	0.029	0.009	—
	0.343	0.365	0.042	9	0.030	0.009	—
	0.372	0.337	0.115	10	0.039	—	—
	0.413	0.304	0.104	8	0.031	—	—
	0.458	0.274	0.042	7	0.022	—	—
	0.488	0.257	0.188	5	0.018	−0.004	—

TABLE 4. Damping rates of ethylene glycol ($Re = 14$) and water ($Re = 295$) bridges calculated according to linear (LT) (Tsamopoulos *et al.* 1992) and nonlinear theory (NT), see CT and experimentally measured (Ex)

Experimental values for damping rates may also be compared with those from linear theory by referring to table 4. It is interesting to note that linear theory for the water bridge at $\Lambda = 0.257$ predicts that the damping rate is very slightly negative, i.e. the bridge is unstable, whereas the bridge was observed experimentally and the damping rate was found to be positive. Apparently, the nonlinear flow field in the bridge modifies its stability characteristics. This requires further investigation of the bridge dynamics close to breakup conditions. Finally, the damping rates of a bridge of mercury with $\Lambda = 0.398$ and 0.503 are found to be much higher than expected and are not shown in figure 9. The larger values for the damping rate of the mercury bridge are suspected to be due to the different wetting conditions on the solid/liquid interface by the mercury. Upon further review of the video tape with experiments using mercury it is found that the bridge in the area around the three-phase contact lines seem to deform and move slightly. In other instances non-axisymmetric shapes are observed. Both are important deviations from the assumed conditions of axisymmetric shapes pinned at the edges of the rods and both lead to significantly higher damping rates, see Tsamopoulos *et al.* (1992) and Borkar & Tsamopoulos (1991).

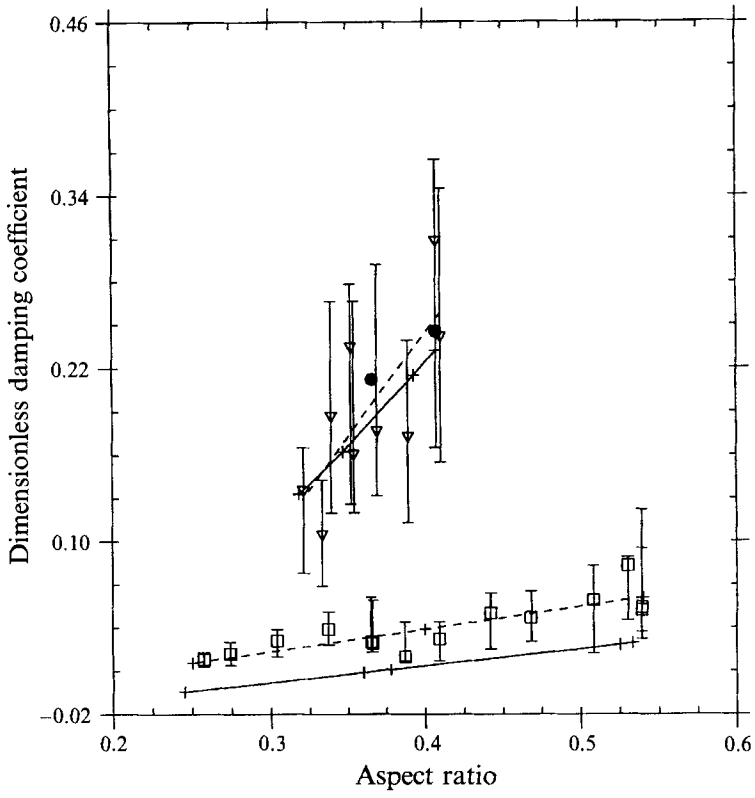

FIGURE 9. Damping coefficients for ethylene glycol (Re = 14) and water (Re = 295). Symbols indicate experimental results for ethylene glycol (▽), water (□), and nonlinear calculations (CT) for ethylene glycol (●) bridges. Results from linear theory for Re = 14 and Re = 295 (+) are connected to form continuous solid curves. The dashed lines result from a linear regression fit to the measured data.

5. Internal flow field

The flow field inside the liquid bridge during forced oscillation of the upper rod is investigated by introducing an aluminium oxide powder as a tracer. The fluid motion is observed by illuminating the zone using two 5 mW He–Ne lasers and observing the light scattered from the particles. Aluminium oxide powder is used because its micron-sized particles provide long settling times and good 90° light scattering. The axisymmetry of the bridge is verified by backlighting the column with a strobe light which is synchronized with its motion (see figure 10). Conventional still photography at 15-fold magnification is employed during the entire flow visualization study. The camera is set up so that the axis of symmetry of the bridge lies on the focal plane of the lense. Short exposure times as low as $\frac{1}{30}$ s are used to capture the small-scale particle motion, and longer exposure times of 1 s are employed to capture the global fluid motion. At 1 s exposure times, for the forcing frequencies of 50–150 Hz discussed here, 50–150 oscillation cycles are captured in each photograph.

In the larger 1 s exposure times of figures 11 and 12, the particles are seen to follow either a single or double toroidal path. The cut of the tori at the focal plane appears to be circular for shorter bridges, but becomes more elongated as the aspect ratio is decreased. The photographs do not have a good contrast at the side boundaries of the bridges due to both continuous deformation of the liquid surface at high speeds and the laser light reflection by the bridge surface.

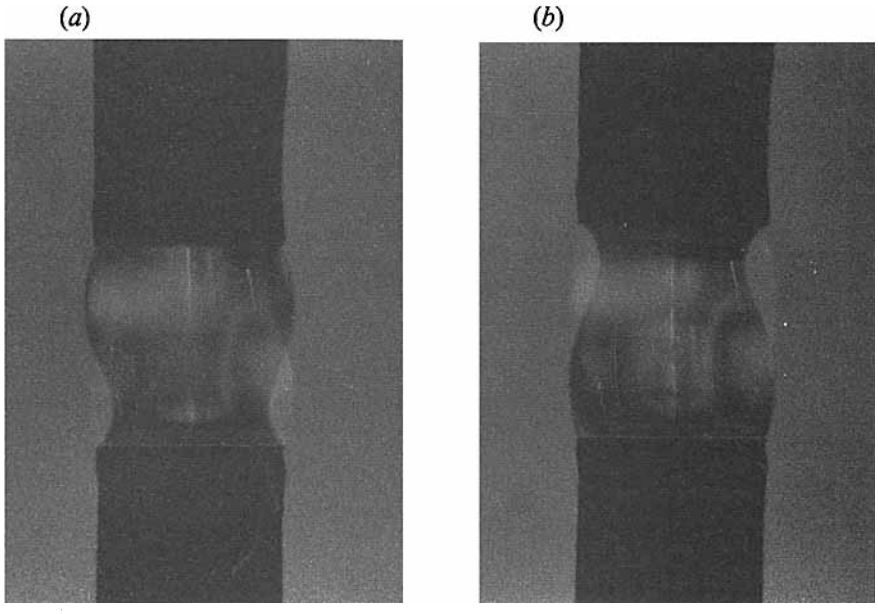

FIGURE 10. Water column excited at 578 rad/s seeded with aluminium oxide, and illuminated with laser light for particle scatter and backlit with synchronized strobe light to show mode shape.

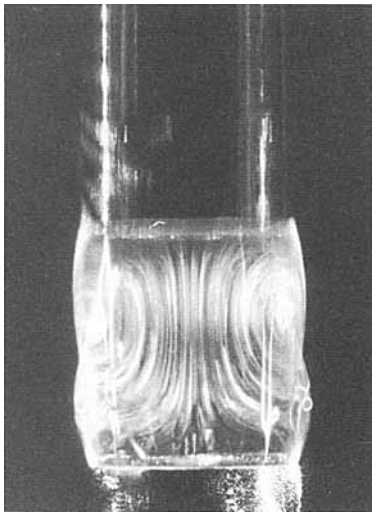

FIGURE 11. Ethylene glycol column seeded with aluminium oxide and illuminated with an He–Ne laser. Conditions are $\bar{\omega} = 622$ rad/s, $Re = 14$, $\Lambda = 0.447$, $B = 0.462$, and $\alpha = 0.09$. Exposure time was $\frac{1}{2}$ s.

Figure 13 is a schematic presentation of the single and double toroidal flow patterns showing the direction of the particle motion. At low Reynolds numbers the liquid circulates throughout the bridge forming the single toroidal structure seen in figure 11. On average, fluid is moving upwards around the bridge centreline and downwards on its free surface. This type of flow results in relatively homogeneous fluid properties throughout the length of the bridge and more effective mass and energy transport between the upper and lower support boundaries. If the excitation amplitude is

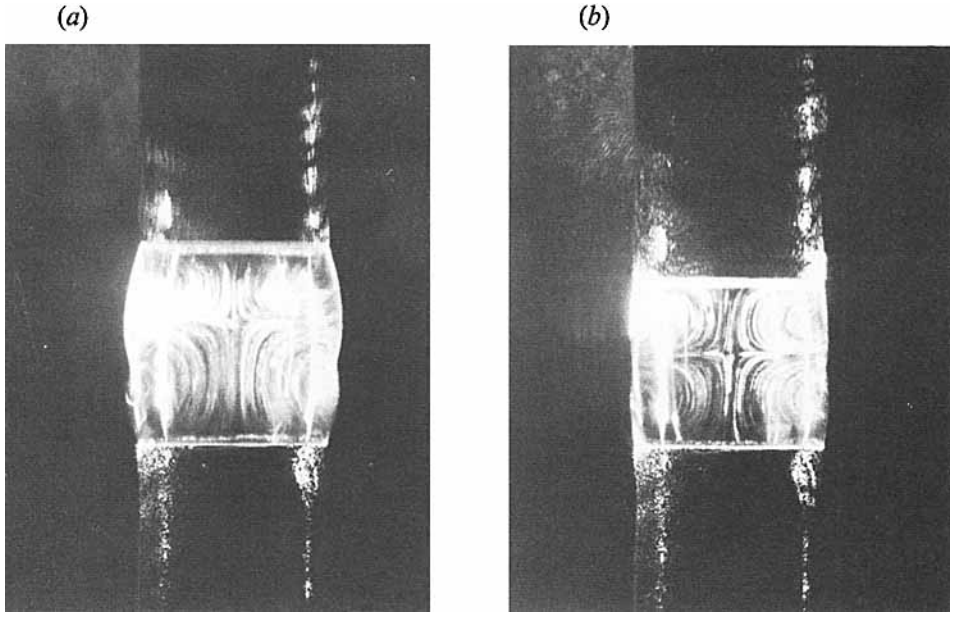

FIGURE 12. Liquid column seeded with aluminium oxide and illuminated with an He–Ne laser. (*a*) Ethylene glycol/water mixture (17%/83% by volume) excited at its first mode resonance frequency, $\bar{\omega} = 622$ rad/s, $Re = 94$, $\Lambda = 0.482$, $B = 0.354$. (*b*) Water column excited at its first mode resonance frequency, $\bar{\omega} = 898$ rad/s, $Re = 295$, $\Lambda = 0.572$, $B = 0.220$. Exposure time for all photographs was 1 s.

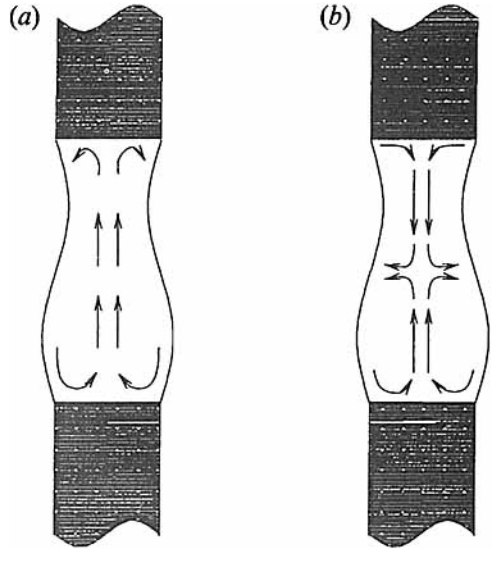

FIGURE 13. Sketch showing the flow pattern and direction of seeded bridges for (*a*) low Reynolds number ($Re \approx 14$) and (*b*) high Reynolds number ($Re \approx 295$).

decreased, the particles near the lower stationary support lose energy faster than the rest of the fluid and stagnate, while the particles closer to the excitation boundary continue their toroidal trajectories.

The genesis of the single toroidal flow structures seen in bridges with a low Reynolds number can be deduced from the instantaneous Eulerian velocity vector plots

presented in figure 8 of CT. These plots are based on the nonlinear analysis presented in that paper for a bridge with $Re = 30$, $\Lambda = 1/\pi$, and $\alpha = 0.2$. One complete cycle of the oscillation at $\frac{1}{6}\pi$ intervals is shown for a liquid bridge which is forced at its nonlinear resonance frequency of the first mode, which is $\sigma = 1.117$.

There is an approximately $\frac{1}{2}\pi$ phase lag between the motion of the upper boundary and the fluid motion in figure 8 of CT (see $t = 1.571$–3.610, and $t = 4.712$–6.283). This phase lag results in an outward average motion over the course of a cycle near the upper boundary of the bridge, and a downward flow on the bridge surface as predicted at $t = 2.121$–3.142. Over the course of many cycles these two dominant velocity fields generate the upward central flow and downward surface flow forming the global recirculation patterns sketched in figure 13(*a*).

In liquids with low modified Reynolds number, overfilling the bridge so that its static shape has a continuous bulge throughout does not disrupt the flow pattern with a single torus. However, as the static bridge shape approaches that of a sphere, rotational modes, made chaotic by surface instabilities of the bridge, rapidly evolve and dominate the flow. The single toroidal structure is unchanged by underfilling the bridge or by changes in excitation amplitude. Furthermore, it is found that an increase in the excitation amplitude results in a significant increase of particle velocity. Again no change in the flow pattern is observed.

In fluids with a higher Reynolds number double toroidal structures are observed as shown in figure 12. The formation of these structures can be explained based on the previously mentioned phase lag between the motion of the excitation boundary and that of the viscous fluid in the bridge. This phase lag results in the generation of two distinct toroidal flow fields moving in opposite directions, one in the upper part of the bridge and one in the lower part. There must be a characteristic *Re* for which the upper toroid becomes observable. As *Re* increases, the upper toroid increases in size and continuously displaces the lower (original) toroid downwards. In fluids with lower Reynolds number the upper toroid does not have enough energy to displace the original one and it is damped out, and only a single toroid is observed. However, as the Reynolds number is increased this new circulatory flow is not completely dissipated over the course of the cycle and the flow near the upper surface forms a small counter-rotating toroid. Figure 12(*a*) shows a double toroidal structure for a column at $Re = 94$. In order to obtain intermediate values of Reynolds numbers, mixtures of water and ethylene glycol are used. The mixture properties are obtained using the relations given in Reid, Prausnitz & Sherwood (1977). As the dissipation is further reduced at the higher Reynolds numbers the upper toroid grows until the upper and lower structures are of the same size, as recorded in figure 12(*b*) for $Re = 295$. Although these bridges with lower viscosity generate higher fluid circulation velocities for a given excitation amplitude, the upper and lower flow fields are isolated, leading to a slower transport of properties between the upper and lower domains.

In contrast to the single toroidal flow pattern, the fluid volume and excitation amplitude affect the structure in the bridges with double toroidal structures. In this case overfilling results in an interaction between the upper and lower toroid and earlier formation of three-dimensional flow patterns. Reducing the excitation amplitude results in a slight increase in the size of the upper toroid relative to the lower one.

In addition to the global toroidal structures, each particle is seen to follow another oscillatory motion at smaller scale. In oscillating liquid bridges, nearly standing (almost fully reflecting) waves are generated at resonance frequency. As the frequency deviates further from resonance the wave increasingly turns into a progressive one. In the latter case the small-scale motion follows an elliptical path, whereas in the nearly

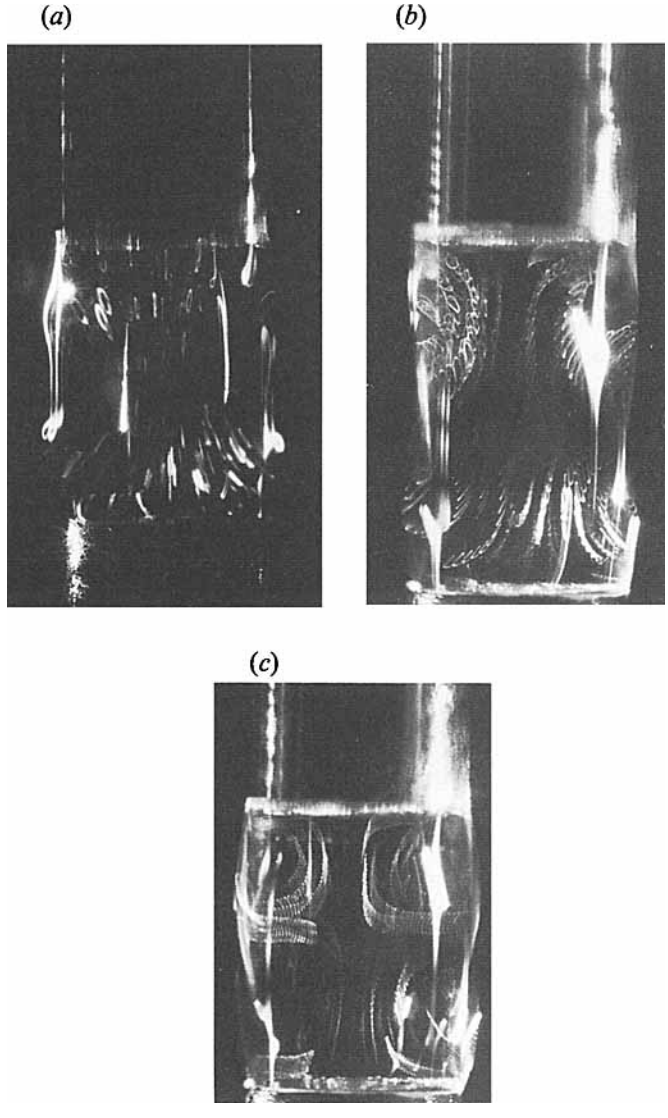

FIGURE 14. Liquid bridges seeded with aluminium oxide powder and illuminated with an He–Ne laser. Bridges are excited off their first mode resonance frequencies to show small-scale elliptical motion of seed particles. (*a*) Ethylene glycol $\bar{\omega} = 364$ rad/s, $Re = 14$, $\Lambda = 0.344$, $B = 0.597$ and exposure time of $\frac{1}{15}$ s. (*b*) Water $\bar{\omega} = 295$ rad/s, $Re = 295$, $\Lambda = 0.313$, $B = 0.402$; and (*c*) water $\bar{\omega} = 502$ rad/s, $Re = 295$, $\Lambda = 0.389$, $B = 0.323$ with exposure times of $\frac{1}{2}$ s.

standing waves each small-scale elliptical path tends to collapse onto a line. This motion is similar to that observed by Ruellan & Wallet (1950) and derived by Stoker (1957) assuming an irrotational flow of an inviscid and incompressible fluid for small amplitude and partially or fully reflecting waves.

In order to observe the small-scale motion, liquid bridges are excited at frequencies off resonance. Figure 14(*a*) is a short-exposure photograph which shows the small-scale elliptical trajectories. Since *Re* is relatively small a single toroid prevails in the large-scale motion. The photographs of figures 14(*b*) and 14(*c*) are at longer exposure times and show the superposition of these elliptical trajectories and the formation of the large-scale toroidal structure. Two toroids are clearly seen in figure 14(*c*) since *Re*

is relatively high. Note, that the axial symmetry of the bridge reduces the radial motion near the centreline resulting in flatter ellipses. Figure 14(*b*) shows wider ellipses than those in figure 14(*c*) owing to its larger deviation from the corresponding resonance frequency.

A better description of the experimentally observed particle trajectories is provided by recasting the calculations by CT from the Eulerian to a Lagrangian reference frame of individual fluid elements at low *Re*. For a given bridge geometry and fluid properties, Eulerian calculations proceed as in CT until a steady oscillatory motion is reached, i.e. all initial transients dissipate. Subsequently, the velocity field and bridge geometry are stored for a complete period of the upper rod oscillation. A number of fluid elements is chosen and their motion is followed for several periods of oscillation. Owing to its periodicity the entire velocity field need not be recalculated when a period is completed. This results in large savings of computation time. For convenience, the fluid elements chosen are initially located at nodes of the finite-element mesh in the mapped domain (see CT). Their mapped coordinates (η_i, ξ_i) and the known interface shape $f(\xi_i, t)$ are used to recover the radial, r_i, and axial, z_i, locations in physical space using the inverse mapping,

$$z_i = \xi_i(1+G(t)), \tag{5.1}$$

$$r_i = \eta_i f(\xi_i, t). \tag{5.2}$$

Using the Eulerian velocity field and the time step, Δt, the position of the particles is updated by the following explicit scheme:

$$z_i(t+\Delta t) = z_i(t)+\alpha A w_i \Delta t, \tag{5.3}$$

$$r_i(t+\Delta t) = r_i(t)+\alpha u_i \Delta t, \tag{5.4}$$

where w_i and u_i are the dimensionless axial and radial velocities, respectively. The dimensionless amplitude of the motion, α, and the aspect ratio, A, arise in (5.3) and (5.4) because velocities are made dimensionless in CT by $\bar{A}\bar{\omega}$, time by $1/\bar{\omega}$, and the radial and axial coordinates by $\bar{R}$ and $\bar{L}$, respectively.

In order to find the velocity of the same particle at its new position $(z_i(t+\Delta t), r_i(t+\Delta t))$, the element in which it is now located must be identified. To this end, first (5.1) and (5.2) are solved for $\xi_i(t+\Delta t)$, and $\eta_i(t+\Delta t)$. Subsequently, velocities are calculated by the finite-element definition

$$u_i(t+\Delta t) = \sum_{j=1}^{9} \phi_j(\xi_i(t+\Delta t), \eta_i(t+\Delta t))\, u_j(t+\Delta t), \tag{5.5}$$

$$w_i(t+\Delta t) = \sum_{j=1}^{9} \phi_j(\xi_i(t+\Delta t), \eta_i(t+\Delta t))\, w_j(t+\Delta t). \tag{5.6}$$

This procedure is repeated for the next time step and for up to 50 periods of oscillation of the upper rod. Figure 15 shows fluid element trajectories in the physical domain for large-amplitude oscillation ($\alpha = 0.2$) near resonance of a viscous liquid ($Re = 20$) and in the absence of gravity. The starting point of each trajectory is indicated by a black dot. Only one half of the plane passing through the axis of symmetry is shown. The other half is symmetric with respect to the axis of symmetry at $r = 0$. During their motion particles are occasionally seen to exceed the vertical line at $r = 1$ or the horizontal line at $z = 1$. This is understandable since the bridge domain also exceeds these limits during motion.

Figure 15(*a–d*) shows the trajectories of four fluid elements initially located in the middle and upper parts of the bridge. The microscale cyclical motion of these particles

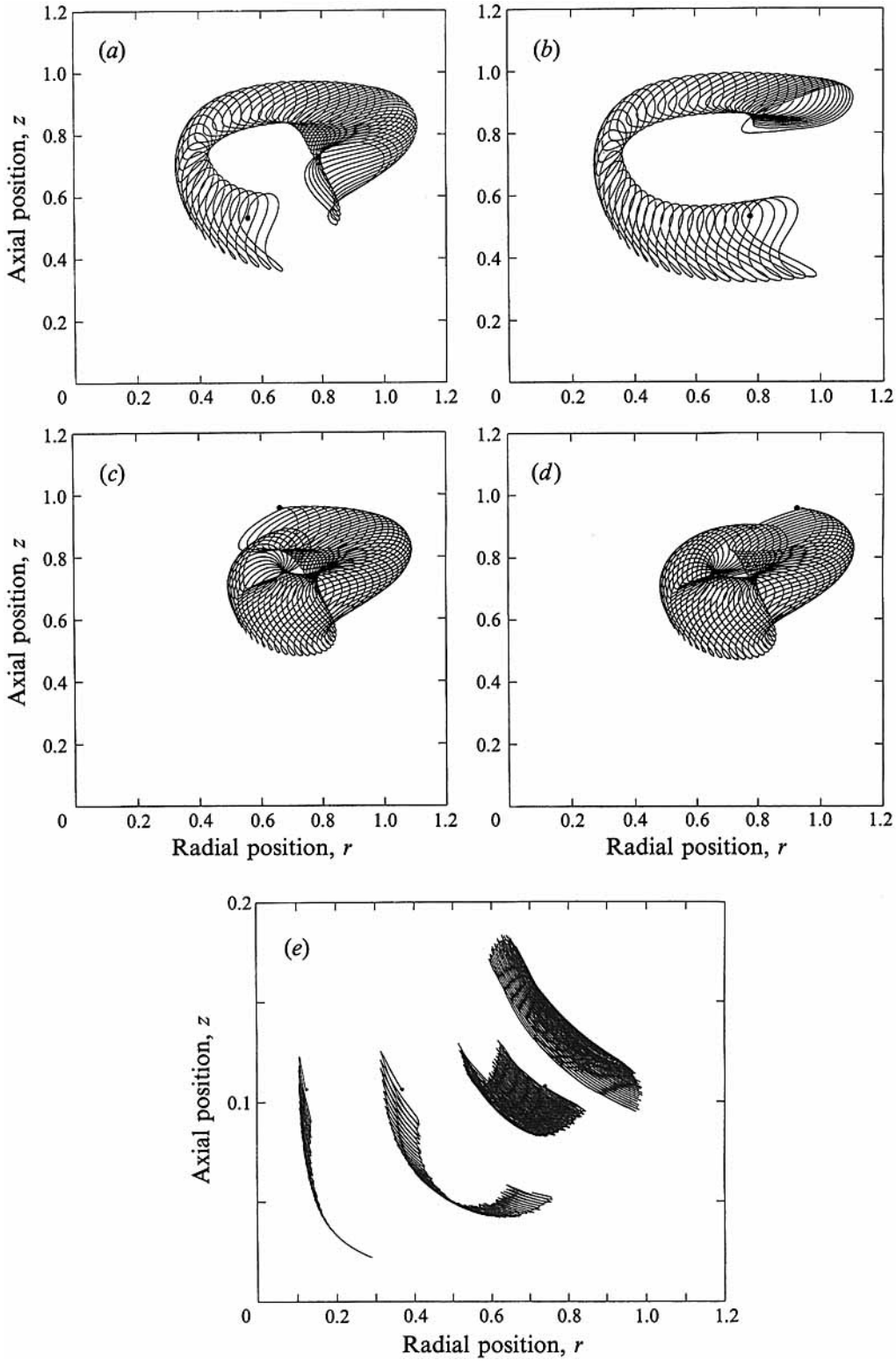

FIGURE 15. Trajectories of fluid elements initially at the point indicated by the black dot, for $\Lambda = 1/\pi$, $\alpha = 0.2$, $Re = 20$, $B = 0$, and $\sigma = 1.15$.

and their macroscale toroidal motion may be readily observed. It was also found, but not shown here, that particles initially located on the axis of symmetry remain there and undergo an oscillation in the vertical direction only. Figure 15(*e*) is an expanded view of trajectories of four particles initially located close to the bottom of the bridge. In contrast to the trajectories of particles above, the microscale motion now looks more like an ellipse with large ratio of its two axes and the macroscale motion will require longer time in order to form the lower region of the toroid. This sharp difference and asymmetry should be expected since it was already found in Eulerian calculations with $Re = 20$ that the energy introduced by the vibrating upper rod dissipates significantly before it reaches the bottom of the bridge. The results calculated above concur with the experimental observations. Additional fluid element trajectories have been calculated for different forcing amplitudes and in the presence of gravity. They are given in Chen (1991).

6. Concluding remarks

An extensive experimental study of the dynamics of liquid bridges is presented. This investigation is aimed at providing experimental data on the resonance frequency and damping rate of capillary bridges and, also, evaluating the prospects of using such data to determine the liquid properties.

A wide range of Reynolds numbers is investigated ($14 \leqslant Re \leqslant 1600$) by using three different fluids. As expected, the first and second mode resonance frequencies increase with aspect ratio. The stronger dependence of the damping coefficient on Reynolds number (at lower Reynolds numbers) is confirmed. Only the damping coefficients for $Re = 14$ and 295 are reported. However, based on the calculations by Tsamopoulos *et al.* (1992) no significant decrease in the damping coefficient is expected at Reynolds numbers greater than 200. The best fit linear curves of the damping coefficients display a more rapid increase in damping with increasing aspect ratio than do their counterparts from the linear model.

The proposed technique for the liquid property determination is based on the experimental measurement of either the resonance frequency or the damping rate of liquid bridges, and subsequent theoretical calculation of the modified Re that provides the same resonance frequency or damping rate. If more than one property is unknown and only resonance frequencies are to be measured, bridges with different aspect ratios must be tested. As noted in Tsamopoulos *et al.* (1992), this technique is applicable to liquids with low modified Re ($Re < 100$).

The technique is validated by applying it to ethylene glycol with $Re = 14$. The resonance frequencies are determined by measuring the surface amplitude of the liquid bridge. Therefore, their accurate determination depends critically on the resolution of the amplitude measurement. In the present experiment using a 240×192 sensor array to record the bridge motion, the maximum amplitude from the static bridge shape corresponds to approximately 7 pixels on the monitor. With 1-pixel resolution, 14% error in the amplitude measurement is expected. Based on the experimental observations, this gives rise to 3% error in the frequency measurement. The frequency values computed by the nonlinear method of CT, for the same geometric and physical parameters as two selected experimental data sets, are indeed within 3% of the mean value of those measured experimentally. The resonance frequencies predicted using the linear theory of Tsamopoulos *et al.* (1992) are consistently about 20% above the measured values. The linear prediction improves to within approximately 16% of the first mode data as bridge length is increased. It can be concluded that the combination

of the experimental determination of the resonance frequency using amplitude measurement with a high resolution, and the nonlinear theory can be used to accurately determine the liquid properties.

The experimental results indicate that the damping rate is more sensitive to the Reynolds number, and therefore, it is a better parameter for the property determination. The damping rate measurements, however, are much more difficult since time-resolved measurements of the amplitude are needed. For more viscous liquids, where the damping rate is higher, the disturbances damp out at a faster rate. For instance, recording the damping of the ethylene glycol bridge at 1000 frames per second results in only 3 to 4 measurable peaks in the amplitude. Therefore, damping rate measurements at such recording speeds results in large errors in determining the liquid properties. Visualization with higher resolutions and faster speeds are needed to properly utilize the damping rate data for property measurement.

Further understanding of the dynamics of liquid bridges is achieved by studying their internal flow fields. Visualization of the internal flow fields showed that the tracers follow complicated circular and toroidal paths. A single toroidal structure is observed at low Reynolds numbers or shorter bridges while a double toroidal structure is established at higher Reynolds numbers or longer bridges. The two toroids are of equal size for very high Reynolds number but the motion of the top toroid cannot be sustained in a more viscous environment and begins to shrink as the Reynolds number is decreased. Using the nonlinear theory of CT, fluid elements in low Reynolds number bridges are followed in time. The paths and directions of travel of these fluid particles agree with the single toroid motion seen in the ethylene glycol bridges.

This work was partially supported by the Fluid Mechanics Program of NSF under grant numbers CTS-9011201 and MSM-8705735. Funds from the later grant contributed to the purchase of the EktaPro 1000 motion analysis system. Usage of the Cornell National Supercomputer Facilities (CNSF) and the graphics software developed by Dr A. Poslinski are gratefully acknowledged.

REFERENCES

BORKAR, A. & TSAMOPOULOS, J. A. 1991 Boundary layer analysis of the dynamics of axisymmetric capillary bridges. *Phys. Fluids* A **3**, 2866–2874.

BROWN, R. A. 1988 Theory of transport processes in single crystal growth from the melt. *AIChE J.* **34**, 881–911.

CHEN, T.-Y. 1991 Static and dynamic analysis of capillary bridges. PhD thesis, Department of Chemical Engineering, State University of New York at Buffalo.

CHEN, T.-Y. & TSAMOPOULOS, J. A. 1993 Nonlinear dynamics of capillary bridges: theory. *J. Fluid Mech.* **255**, 373–409 (referred to herein as CT).

CHEN, T.-Y., TSAMOPOULOS, J. A. & GOOD, R. J. 1992 Capillary bridges between parallel and non-parallel surfaces and their stability. *J. Colloid Interface Sci* **151**, 49–69.

FOWLE, A. A., WANG, C. A. & STRONG, P. F. 1979 Experiments on the stability of conical and cylindrical liquid columns at low Bond numbers. *Arthur D. Little Co.* Ref. C-82435.

LAPLACE, P. S. 1805 Theory of capillary attractions, supplement to the *Tenth Book of Celestial Mechanics* (translated and annotated by N. Bowditch, 1839). Reprinted by Chelsea, New York, 1966.

MASON, G. 1970 An experimental determination of the stable length of cylindrical liquid bridges. *J. Colloid Interface Sci.* **32**, 172–176.

MELROSE, J. C. 1966 Model calculations for capillary condensation. *AIChE J.* **12**, 986–994.

MESEGUER, J. 1983 The breaking of axisymmetric slender liquid bridges. *J. Fluid Mech.* **130**, 123–151.

PLATEAU, J. A. F. 1863 Experimental and theoretical researchers on the figures of equilibrium of a liquid mass withdrawn from the action of gravity. Translated in *Ann. Rep. Smithsonian Inst.*, pp. 207–285.

PREISER, F., SCHWABE, D. & SCHARMANN, A. 1983 Steady and oscillatory thermocapillary convection in liquid columns with free cylindrical surface. *J. Fluid Mech.* **126**, 545–567.

RAYLEIGH, LORD 1879 On the instability of jets. *Proc. Lond. Math. Soc.* **10**, 4–13.

RAYLEIGH, LORD 1892 On the stability of cylindrical fluid surfaces. *Phil. Mag.* **34**, 177–180.

REID, R. C., PRAUSNITZ, J. M. & SHERWOOD, T. K. 1977 *The Properties of Gases and Liquids.* McGraw-Hill.

RIVAS, D. & MESEGUER, J. 1984 One-dimensional self-similar solution of the dynamics of axisymmetric slender liquid bridges. *J. Fluid Mech.* **138**, 417–429.

RUELLAN, F. & WALLET, A. 1950 Trajectoires internes dans un clapotis particl. *La Houille Blanche* **5**.

SANZ, A. 1985 The influence of the outer bath in the dynamics of axisymmetric liquid bridges. *J. Fluid Mech.* **156**, 101–140.

STOKER, J. J. 1957 *Water Waves.* Interscience.

TRINH, E. H., MARSTON, P. L. & ROBEY, J. L. 1988 Acoustic measurement of the surface tension of levitated drops. *J. Colloid Interface Sci.* **124**, 95–103.

TSAMOPOULOS, J. A., CHEN, T.-Y. & BORKAR, A. 1992 Viscous oscillations of capillary bridges. *J. Fluid Mech.* **235**, 579–609.

YOUNG, T. 1805 Essay on the cohesion of fluids. *Phil. Trans. R. Soc. Lond.* A **306**, 347–370.

ZASADZINSKI, J. N., SWEENEY, J. B., DAVIS, H. T. & SCRIVEN, L. E. 1987 Finite element calculation of fluid menisci and thin-films in model porous media. *J. Colloid Interface Sci.* **119**, 108–116.